

Slope-assisted Raman distributed optical fiber sensing

JIAN LI,^{1,2} XINXIN ZHOU,² YANG XU,² LIJUN QIAO,² JIANZHONG ZHANG,¹ AND MINGJIANG ZHANG^{1,2,*}

¹College of Physics and Optoelectronics, Taiyuan University of Technology, Taiyuan 030024, China

²Key Laboratory of Advanced Transducers and Intelligent Control Systems (Ministry of Education and Shanxi Province), Taiyuan University of Technology, Taiyuan 030024, China

*Corresponding author: zhangmingjiang@tyut.edu.cn

Received 2 September 2021; revised 1 November 2021; accepted 9 November 2021; posted 11 November 2021 (Doc. ID 442352); published 21 December 2021

Raman distributed optical fiber sensing is required to achieve accurate temperature measurements in a micro-scale area. In this study, we first analyze and demonstrate the pulse transmission feature in the temperature variation area and the superposition characteristics of Raman optical time-domain reflectometry (OTDR) signals by numerical simulation. The equations of superimposed Raman anti-Stokes scattered signals at different stages are presented, providing a theoretical basis for the positioning and physical quantity demodulation of whole optical fiber systems based on the OTDR principle. Moreover, we propose and experimentally demonstrate a slope-assisted sensing principle and scheme in a Raman distributed optical fiber system. To the best of our knowledge, this is the first experimental demonstration of Raman distributed optical fiber sensing in a centimeter-level spatial measurement region. © 2021 Chinese Laser Press

<https://doi.org/10.1364/PRJ.442352>

1. INTRODUCTION

Over the last decade, distributed optical fiber sensing has increasingly attracted the attention of researchers [1–5], as it provides the ability to detect, along with sensing fiber lines, the spatial distribution of surrounding environmental quantities such as temperature [1,2], strain [3,5], vibration [6–8], magnetic fields [9], and gases [10,11]. Based on the physical quantities monitored above, distributed optical fiber sensing has been widely used in micro-/nano-sensing [12], medical treatment [13], corrosion environment detection [14], pressure sensing in harsh environments [15], hydrophone sensors [16], and other security detection fields.

Distributed optical fiber sensing based on the classification of scattering mechanisms can be divided into Rayleigh optical fiber sensing [17,18], Brillouin optical fiber sensing [19,20], and Raman optical fiber sensing [21,22]. Raman distributed fiber sensing is a typical optical fiber sensor that operates on the principle that spontaneous Raman scattering is excited by a pulsed laser in an optical fiber [23]. It has been widely used in the linear infrastructure temperature detection field owing to its advantages of fast measurement speed, simple structure, and temperature sensitivity [24]. With the help of advanced schemes, the sensing range of Raman distributed fiber sensing can reach from several kilometers [25] up to a few tens of kilometers [26]. Consequently, it can realize temperature sensing at any point along tens of kilometers of fiber. However, the temperature demodulation data is the average over an entire fiber

length equal to the spatial resolution, owing to the limitations of pulse width and the principle of optical time-domain reflectometry (OTDR) [27]. Thus, the temperature detection result is much smaller than the true temperature when the detection area is smaller than the spatial resolution of the system. For example, in a temperature detection area of 1.0 cm (the temperature being approximately 200°C), the detected temperature using the conventional measurement method is 35.6°C (with a spatial resolution of 1.0 m), the measurement error reaching several hundred degrees Celsius. Consequently, the temperature values obtained can be significantly underestimated when the size of the temperature variation spot along the fiber is small. Subsequently, pre-warning of anomalous temperature points and fires could be delayed, leaving less time for fire departments to react. Therefore, temperature detection in small-scale areas is of great importance for the reliable detection of small anomalous spots in applications such as gas production [24] and fire prediction [26].

Several advanced demodulation methods have been developed to solve these problems [28–32] and can typically be divided into two categories, that is, one category which attempts to improve the spatial resolution of the system [28–30] and a second category which uses the sensing fiber as a sensing network to avoid limitations of the spatial resolution of measurement results [31,32]. In the first category, special fiber sensing [28], optical pulse coding [29], and time-domain differential correlation demodulation [30] are regarded as effective

methods for optimizing the spatial resolution. For example, Liu *et al.* proposed a graded-index few-mode fiber (FMF) sensing in 2018 to enhance the spatial resolution, with the experiment results demonstrating spatial resolution performance of 1.04 and 2.58 m at 19.09 and 21.7 km, respectively [28]. Scott *et al.* combined a low-repetition-rate quasi-periodic pulse coding scheme with Raman distributed fiber sensing, achieving a spatial resolution of 1.0 m over 26.0 km [29]. This was the best spatial resolution achieved under experimental conditions at such long sensing distances. Furthermore, a reconstruction compression correlation demodulation scheme for Raman distributed fiber sensing was demonstrated in our previous work [30], a spatial resolution of 7.5 mm being demonstrated along a 10.0 km sensing fiber in 2021. However, because of the avalanche photodiode's limited bandwidth, this scheme could not be experimentally realized. At present, the best achievable spatial resolution has been limited to the order of meters when operating over long sensing ranges [27]. Unfortunately, the existing spatial resolution means that accurate temperature detection cannot be achieved in small-scale areas. Pandian *et al.* discussed a methodology for increasing the capability of small-scale temperature monitoring using a single-fiber grid [31]. Sun *et al.* proposed a parallel optical fiber method as the sensing element, which could achieve accurate positioning over a small-scale range [32]. However, these methods could only achieve positioning but could not obtain accurate temperature information.

In this paper, we propose a novel optical scheme called slope-assisted sensing to improve the capability of temperature monitoring in micro-scale regions. The proposed scheme has two innovations. First, an accurate temperature measurement in a region of 1.0 cm spatial scale—even if the spatial resolution of the system was of the order of a meter—was experimentally demonstrated. The proposed scheme could eliminate expensive pulse-encoding sources and special sensing fibers compared to advanced schemes, thereby confirming the utility of the technique in practical applications. Second, the pulse transmission feature in the temperature variation area of the sensing fiber and superposition characteristics of the Raman OTDR signal were first theoretically analyzed and simulated. The equations of superimposed Raman anti-Stokes scattered signals were derived at different stages. Consequently, the theoretical analysis performed in the current study could be a useful tool for designing distributed optical fiber sensors based on the OTDR principle, such as Brillouin optical time domain reflectometry (BOTDR), Brillouin optical time-domain analysis (BOTDA), and Rayleigh-OTDR systems.

2. METHODOLOGY: PRINCIPLE AND NUMERICAL SIMULATION

A. Pulse Transmission and Superposition Characteristics of Raman Scattered Signal

First, we studied the transmission features of the pulsed laser in the temperature variation area of a sensing fiber and the superposition characteristics of the Raman scattered intensity. In Raman distributed optical fiber sensing, the positioning and acquisition of the system are based on the OTDR principle, which means that the Raman anti-Stokes scattered signal

(hereafter referred to as the Raman signal) collected by the system at a certain moment comprises the superposition of the entire scattered intensity data in a section of the sensing fiber, the length of this section being related to the pulse width. The intensity collected at a position L is an intensity superposition with the length of the interval $(L - W_c/2n \sim L)$, where W_c is the pulse width, and n is the refractive index of the optical fiber.

The pulse transmission trajectory can be divided into the following four parts when the pulsed laser is transmitted in the temperature-variation region of the sensing fiber, including the fiber under test (FUT) area and non-FUT area, as shown in Fig. 1. First, the pulsed laser is transmitted in the non-FUT area (from A to B). The Raman intensity collected by this area comprises the superimposed intensity within the pulse width interval, which can be expressed as follows:

$$\phi_a(L_{AB}) = \sum_{L_j=L_i}^{L_f} \{K_a \lambda_a^{-4} P \times R_a(T_{\text{non-FUT}}) \times \exp[-(\alpha_o + \alpha_a)L_j]\}. \quad (1)$$

The parameters for the Raman anti-Stokes signal are listed in Table 1. The superimposed intensity is related to several inherent parameters of the fiber, such as the incident power, fiber attenuation, and temperature of the non-FUT area. Because the temperature in this area remains essentially constant, the superimposed intensity of the Raman signal is dynamically modulated by the fiber attenuation, which gradually decreases

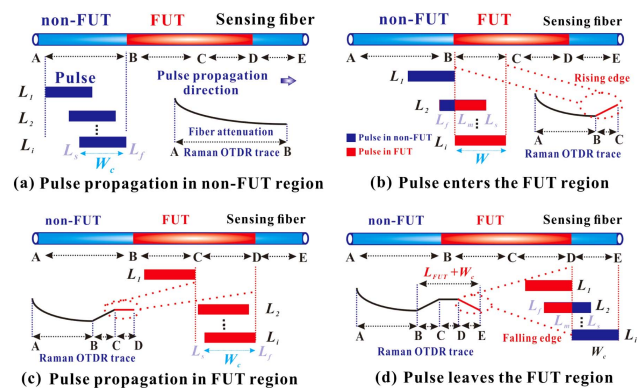


Fig. 1. Schematic diagram of the pulse transmission and characteristics of the superimposed Raman signals.

Table 1. Parameters for the Superimposed Raman Signal

Parameters	Symbol
Raman scattering coefficient	K_a
Anti-Stokes wavelength	λ_a
Incident light power	P
Temperature coefficient	$R_a(T)$
Attenuation coefficient	$\alpha_o + \alpha_a$
Starting position of the pulse	L_i
Final position of the pulse	L_f

with increasing sensing distance, as shown in the schematic diagram of the Raman OTDR trace in Fig. 1(a).

Furthermore, the superimposed intensity of the Raman signal contains two parts—that is, when the pulsed laser enters the FUT region (the temperature of the FUT is higher than that of the non-FUT). As shown in Fig. 1(b), the superimposed intensity includes the intensity of the FUT area (from L_s to L_m) and the intensity of the non-FUT area (from L_m to L_f). The superimposed intensity of the Raman signal in this area can be expressed as follows:

$$\begin{aligned} \phi_a(L_{BC}) = & \sum_{L_i=L_s}^{L_m} \{K_a \lambda_a^{-4} P \times R_a(T_{\text{FUT}}) \times \exp[-(\alpha_o + \alpha_a)L_i]\} \\ & + \sum_{L_i=L_m}^{L_f} \{K_a \lambda_a^{-4} P \times R_a(T_{\text{non-FUT}}) \\ & \times \exp[-(\alpha_o + \alpha_a)L_i]\}. \end{aligned} \quad (2)$$

Because part of the superimposed intensity collected in this area is modulated by the temperature of the FUT, its superimposed intensity is stronger than that of the superimposed Raman signal collected in the non-FUT. The pulsed signal is gradually incident into the FUT area, meaning that the superimposed intensity gradually increases with the sensing distance until the pulsed laser fully enters the FUT area, as shown in the schematic diagram of the Raman OTDR trace in Fig. 1(b). The rising edge of the Raman OTDR curve in the FUT occurs during this stage. Most importantly, the spatial length of this region is the minimum value of the pulse width and the FUT length.

When the pulsed laser is completely transmitted in the FUT area (from C to D), as shown in Fig. 1(c), the superimposed intensity of the Raman signal depends mainly on the temperature of the FUT and can be expressed as follows:

$$\phi_a(L_{CD}) = \sum_{L_i=L_s}^{L_f} \{K_a \lambda_a^{-4} P \times R_a(T_{\text{FUT}}) \times \exp[-(\alpha_o + \alpha_a)L_i]\}. \quad (3)$$

Because the temperature of the FUT remains constant, the superimposed intensity collected in this area remains constant. Moreover, the superimposed Raman OTDR curve shows that the spatial length of this area is the difference between the FUT length and the pulse width ($L_{CD} = L_{\text{FUT}} - W_c$) when the FUT length is greater than the pulse width. Finally, as shown in Fig. 1(d), the superimposed Raman signal excited by this area can also be regarded as comprising two parts, when the pulsed laser gradually leaves the FUT area (from D to E)—that is, it includes the Raman signal in the non-FUT and FUT areas. The superimposed intensity shows a gradually decreasing trend with the increase in sensing distance until the pulsed laser completely leaves the FUT area, and can be expressed as follows:

$$\begin{aligned} \phi_a(L_{DE}) = & \sum_{L_i=L_s}^{L_m} \{K_a \lambda_a^{-4} P \times R_a(T_{\text{non-FUT}}) \times \exp[-(\alpha_o + \alpha_a)L_i]\} \\ & + \sum_{L_i=L_m}^{L_f} \{K_a \lambda_a^{-4} P \times R_a(T_{\text{FUT}}) \times \exp[-(\alpha_o + \alpha_a)L_i]\}. \end{aligned} \quad (4)$$

The falling edge of the superimposed Raman OTDR curve in the FUT area is formed during this stage, and the spatial length of this area is the minimum value of the pulse width and the FUT length. Most importantly, based on the aforementioned pulse transmission and superposition characteristics, it can provide a theoretical basis for the positioning and physical quantity demodulation of whole systems based on the OTDR principle, such as the BOTDR, BOTDA, and Rayleigh-OTDR systems.

B. Numerical Simulation

We designed a numerical simulation model to verify the above-mentioned theories, the simulation model being shown in Fig. 2. A 10.0 km sensing fiber (with temperature of 25.0°C) was used, in which a section of 2.0 m FUT was set at a position of 10.0 km as a temperature variation region, its temperature being set at 80.0°C. Pulsed lasers of pulse-widths 30, 20, and 10 ns (and wavelength 1550 nm) were injected into the sensing fiber. The Raman anti-Stokes scattered signal (of wavelength 1450 nm) was filtered out by a wavelength division multiplexer (WDM) and collected by an acquisition and demodulation system.

The simulated Raman signals are shown in Fig. 3(a). As mentioned previously, the Raman OTDR curves collected in the experiment represent the superposition of the light intensity within the pulse width scale, the superimposed intensity collected at a certain moment being related to the pulse width—that is, the wider the pulse width, the stronger the superimposed Raman intensity under the same conditions. The simulation results also confirmed that the superimposed intensity based on a pulse width of 30 ns was stronger than that based on a pulse width of 20 and 10 ns. Figure 3(b) shows the excited Raman OTDR signal based on a 10 ns pulse width. In this case, the pulse width was less than the length of the actual FUT.

The transmission trajectory includes four stages. The first stage is the transmission of the pulsed laser in the non-FUT (from A to B). The superimposed Raman OTDR trace shows a gradually decreasing trend, with an increase in the sensing distance due to fiber attenuation. In the second stage, the pulsed laser gradually enters the FUT area (from B to C), the superimposed intensity excited in this area containing the Raman signal in the FUT and non-FUT areas. Consequently, the superimposed intensity shows a gradual increase during this stage. The third stage is the transmission of the pulsed laser in the FUT area (from C to D). Because the temperature of the FUT area remains constant in the model, the superimposed intensity excited in this area remains constant. In the fourth

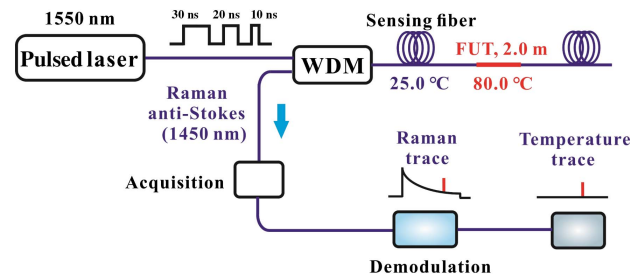


Fig. 2. Numerical simulation model.

stage, the pulsed laser gradually leaves the FUT area (from D to E), the Raman signal in this area comprising the superimposed intensity excited by the non-FUT and the FUT areas. Here, the difference is that as the sensing distance increases, the proportion of the Raman signal excited by the non-FUT region collected in this region gradually increases, the superimposed intensity exhibiting a gradual decrease during this stage. The simulation results show that the excited Raman OTDR signal is consistent with the aforementioned theory of our analysis.

Figures 3(c) and 3(d) show the Raman signals excited by the pulsed laser under pulse widths of 20 and 30 ns, respectively. In Fig. 3(c), the length of the FUT is 2 m, which is consistent with the spatial scale of the 20 ns pulse width. Consequently, when the entire pulsed laser is transmitted to the FUT area, the spatial scale of it is exactly the same as the spatial length of the FUT. Compared to the Raman OTDR curves excited by a pulse width of 10 ns, the transmission signal of the pulsed laser is submerged at a distance from C to D . When the spatial scale of the pulse width is greater than the length of the FUT, the excited Raman signal is as shown in Fig. 3(d). Compared to the other two scenarios, when the pulse width is less than the area length and when the front end of the laser reaches the end of the FUT area, the pulsed laser is completely contained within the FUT area.

Based on this theoretical analysis and the simulation results, we studied the dynamic response characteristics of superimposed Raman OTDR traces with different pulse widths in the FUT region. First, the spatial length of the superimposed intensity influenced by the FUT area was longer than the actual length of the FUT area. The results showed that the spatial length of the superimposed Raman OTDR trace affected by the FUT area was the FUT length plus the pulse width. As shown in Fig. 3, the light blue areas represent the actual spatial length and position of the FUT area. This shows that the superimposed Raman OTDR signal modulated by the FUT temperature does not fully map the position and length of the actual FUT area. The true position corresponding to the falling edges of the Raman OTDR curve excited by pulse widths of 10 and

20 ns is in the non-FUT region. Based on this, we can see from Fig. 3 that the spatial spans of the rising or falling edges of the Raman OTDR traces in the FUT area are determined by the minimum value between the pulse width and FUT length.

Consequently, when the pulse width of the system is determined, the length and position of the actual FUT can be calculated using the spatial length of the rising edge of the Raman OTDR curve. Furthermore, the measurement accuracy is related to the pulse width and the FUT length. Specifically, when the pulse width is less than the length of the FUT, the region [from C to D in Fig. 3(a)] can accurately demodulate the temperature information. When the pulse width is equal to the length of the FUT, the actual temperature information can only be detected at one point [at position C in Fig. 3(b)]. When the pulse width is greater than the length of the FUT, the entire Raman OTDR trace cannot accurately detect the temperature information. This is because the superimposed intensity excited in this area contains a superimposed signal in the FUT and non-FUT areas. Unfortunately, the system assumes that the Raman signals collected in this area are modulated by the signals of the FUT area. When the length of the FUT area is very small, the effective intensity is submerged in the non-FUT area, leading to significant measurement errors—that is, the OTDR principle leads to a temperature-detection result that is much smaller than its true temperature when the detection area is smaller than the spatial resolution of the system. This can limit temperature-monitoring capabilities in small-scale regions for whole optical fiber sensing systems based on the OTDR principle.

C. Slope-Assisted Temperature Demodulation Scheme

We propose a slope-assisted temperature sensing scheme based on the aforementioned pulse transmission and superposition characteristics of scattering signal. In the proposed slope-assisted demodulation scheme, we defined the part of the falling edge of the Raman OTDR curve as the slope-assisted detection area. The distance span within this area is from the point when the pulse laser starts to exit from the FUT area to when it leaves the FUT area completely. In the slope-assisted detection area, the collected data includes the intensity information of the FUT and non-FUT areas. Figure 4 illustrates the principle of the slope-assisted sensing scheme. As can be surmised from

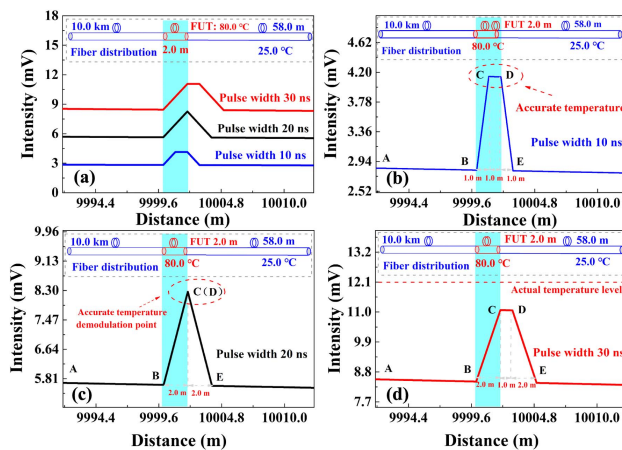


Fig. 3. Superimposed Raman OTDR traces under different pulse widths. (a) Whole superimposed Raman OTDR traces. Superimposed Raman OTDR traces based on (b) 10 ns pulse width, (c) 20 ns pulse width, and (d) 30 ns pulse width.

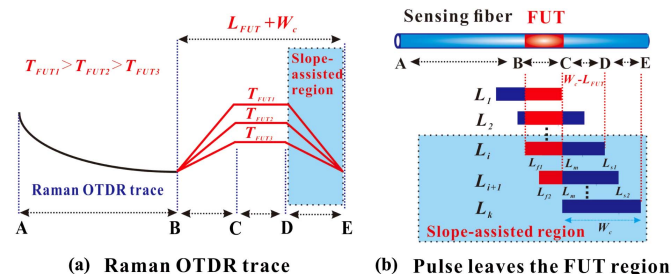


Fig. 4. Schematic diagram based on the slope-assisted demodulation scheme (L_{FUT} is the true length of the FUT). (a) Superimposed Raman OTDR traces at different FUT temperatures. (b) Schematic diagram of pulse transmission in the slope-assisted area when pulse width is greater than the length of the FUT.

Fig. 4(a), the larger the temperature difference between the FUT and non-FUT areas, the faster the Raman OTDR curve of the slope-assisted area decreases. The temperature variation causes different falling slopes in the slope-assisted region, which is the basic principle on which the proposed slope-assisted demodulation method is based.

The temperature demodulation process of the slope-assisted scheme can be explained as follows: to extract the slope-assisted coefficient, the demodulation system requires at least two pieces of Raman intensity data in the slope-assisted detection area, as shown in Fig. 4(b). The superimposed intensity of the Raman signal collected at position L_i can be expressed as follows:

$$\begin{aligned} \phi_a(L_i) = & \sum_{i=L_{i1}}^{L_m} \{K_a \lambda_a^{-4} P \times R_a(T_{\text{non-FUT}}) \times \exp[-(\alpha_o + \alpha_a)L_i]\} \\ & + \sum_{i=L_m}^{L_{f1}} \{K_a \lambda_a^{-4} P \times R_a(T_{\text{FUT}}) \times \exp[-(\alpha_o + \alpha_a)L_i]\}. \end{aligned} \quad (5)$$

This is the first valid data for slope-assisted demodulation. Furthermore, the superimposed intensity of the Raman signal collected by position L_{i+1} (the next collection point), belonging to the second valid dataset, can be expressed as follows:

$$\begin{aligned} \phi_a(L_{i+1}) = & \sum_{i=L_{i2}}^{L_m} \{K_a \lambda_a^{-4} P \times R_a(T_{\text{non-FUT}}) \times \exp[-(\alpha_o + \alpha_a)L_i]\} \\ & + \sum_{i=L_m}^{L_{f2}} \{K_a \lambda_a^{-4} P \times R_a(T_{\text{FUT}}) \times \exp[-(\alpha_o + \alpha_a)L_i]\}. \end{aligned} \quad (6)$$

Based on these two pieces of data, the slope-assisted coefficient can be calculated. However, before demodulation, we have to pre-calibrate these two pieces of data. From Eqs. (5) and (6), we can see that several inherent parameters of the fiber ($K_a, \lambda_a, \alpha_o, \alpha_a$, etc.) also modulate the superimposed intensity of the Raman signal. To compensate for the influence of these parameters on the temperature demodulation results, the entire sensing fiber needs to be placed in a constant temperature field (T_o) for calibration before temperature measurement. During the calibration process, the superimposed intensity of the Raman signal based on a single pulse can be expressed as follows:

$$\phi_{ao}(L_i) = \sum_{i=L_s}^{L_f} \{K_a \lambda_a^{-4} P \times R_a(T_o) \times \exp[-(\alpha_o + \alpha_a)L_i]\}. \quad (7)$$

After the calibration process (superimposed Raman anti-Stokes intensity in the measurement phase and superimposed Raman anti-Stokes intensity in the calibration phase), the superimposed Raman intensities of the acquisition of positions L_i and L_{i+1} can be expressed by Eqs. (8) and (9), respectively, as follows:

$$\begin{aligned} \frac{\phi_a(L_i)}{\phi_{ao}(L_i)} = & \sum_{L_{i1}}^{L_m} \left[\frac{R_a(T_{\text{non-FUT}})}{R_a(T_o)} \right] + \sum_{L_m}^{L_{f1}} \left[\frac{R_a(T_{\text{FUT}})}{R_a(T_o)} \right] \\ = & \sum_{L_{i1}}^{L_m} \left[\frac{\exp(h\Delta v/kT_o - 1)}{\exp(h\Delta v/kT_{\text{non-FUT}} - 1)} \right] \\ & + \sum_{L_m}^{L_{f1}} \left[\frac{\exp(h\Delta v/kT_o - 1)}{\exp(h\Delta v/kT_{\text{FUT}} - 1)} \right], \end{aligned} \quad (8)$$

$$\begin{aligned} \frac{\phi_a(L_{i+1})}{\phi_{ao}(L_{i+1})} = & \sum_{L_{i2}}^{L_m} \left[\frac{R_a(T_{\text{non-FUT}})}{R_a(T_o)} \right] + \sum_{L_m}^{L_{f2}} \left[\frac{R_a(T_{\text{FUT}})}{R_a(T_o)} \right] \\ = & \sum_{L_{i2}}^{L_m} \left[\frac{\exp(h\Delta v/kT_o - 1)}{\exp(h\Delta v/kT_{\text{non-FUT}} - 1)} \right] \\ & + \sum_{L_m}^{L_{f2}} \left[\frac{\exp(h\Delta v/kT_o - 1)}{\exp(h\Delta v/kT_{\text{FUT}} - 1)} \right]. \end{aligned} \quad (9)$$

We can see that several inherent parameters of the optical fiber have been eliminated. The slope-assisted coefficient of the FUT can be calculated using Eq. (10) through Eqs. (8) and (9), as follows:

$$\begin{aligned} \phi_{\text{slope}} = & \frac{\frac{\phi_a(L_{i+1})}{\phi_{ao}(L_{i+1})} - \frac{\phi_a(L_i)}{\phi_{ao}(L_i)}}{L_{i+1} - L_i} = \frac{\sum_{L_{i1}}^{L_{i2}} \left[\frac{\exp(h\Delta v/kT_o - 1)}{\exp(h\Delta v/kT_{\text{non-FUT}} - 1)} \right]}{L_{i+1} - L_i} \\ & - \frac{\sum_{L_{f1}}^{L_{f2}} \left[\frac{\exp(h\Delta v/kT_o - 1)}{\exp(h\Delta v/kT_{\text{FUT}} - 1)} \right]}{L_{i+1} - L_i}, \end{aligned} \quad (10)$$

where T_o, L_n , and L_{n+1} are constants, and $T_{\text{non-FUT}}$ can be calculated using conventional temperature demodulation methods. As such, the slope-assisted coefficient (Φ_{slope}) and temperature of the FUT area (T_{FUT}) exhibit a definite functional relationship. Based on this functional relationship, the actual temperature information along the FUT can be demodulated. The traditional demodulation process does not consider the influence of signal superposition, which causes the effective temperature signal to be submerged in the collected average data. In our proposed scheme, we extract the temperature variation information based on the slope of the Raman OTDR curve in the slope-assisted area instead of the traditional intensity demodulation. Compared with traditional Raman distributed optical fiber sensing, the scheme proposed in this paper can eliminate the problem of signal crosstalk due to the OTDR position principle. It also solves the technical problem whereby traditional demodulation systems have difficulty identifying the characteristics of the environmental temperature change in a micro-scale area.

3. EXPERIMENTAL SETUP AND RESULTS

A. Experimental Setup

The experimental setup, based on slope-assisted Raman distributed fiber sensing, is shown in Fig. 5. The system comprised a distributed feedback (DFB) laser, semiconductor optical amplifier (SOA), WDM, high-speed data acquisition card (DAC),

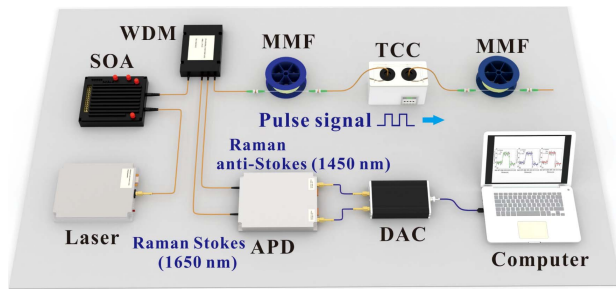


Fig. 5. Experimental setup based on slope-assisted demodulation sensing.

and avalanche photo diode (APD). The pulsed laser source (DFB laser and SOA) operated at a wavelength of approximately 1550 nm and a repetition rate of 6 kHz. Pulses with a peak optical power of 15 W were launched into the sensing fiber (graded-index multimode, 62.5/125, MMF). The back-scattered light from the WDM was separated into anti-Stokes and Stokes signals, which were then detected simultaneously using low-noise APDs. Next, the electrical signals were collected by a DAC before being transmitted to a computer for further data processing.

B. Temperature-Measurement Results Based on Slope-Assisted Demodulation

We experimentally conducted a temperature measurement based on the slope-assisted demodulation scheme. A section of the FUT (of length 5.0 m) at a position of 487.0 m was set up as the temperature variation region, the length of the entire sensing fiber being 900.0 m. Pulsed lasers of different pulse widths (30.30, 45.45, and 53.03 ns, respectively) were then injected into the FUT (5.0 m). Among them, the collected effective Raman signal excited under each pulse width was processed 10,000 times by the accumulation average. The temperature of the FUT was set at 39.77°C, 42.37°C, 48.40°C, 52.39°C, 56.36°C, and 60.55°C using a high-precision temperature chamber controller (TCC). The remaining non-FUT area was placed in a room temperature environment (25.5°C). Subsequently, the DAC and computer started collecting and demodulating the superimposed Raman signals excited along the FUT.

The Raman signals collected after attenuation compensation based on Eq. (8) are shown in Fig. 6. Figures 6(a1)–6(a3) show the superimposed Raman OTDR trace excited by the pulsed laser incident on the FUT area under different pulse widths. After attenuation compensation under constant temperature conditions, the superimposed intensity of the non-FUT region was unaffected by the pulse width. When the spatial length of the pulse width was greater than the length of the FUT—such as the pulse width with 53.03 ns—the intensity of the Raman signal in the FUT area was weaker than that of the Raman signals excited by the pulse width of 30.30 and 45.45 ns. Moreover, compared with the simulation results shown in Fig. 3, the rising and falling edges of the Raman OTDR curve in the FUT region were not smooth. This was because—owing to the light source equipment limitations—the pulsed laser injected into the FUT area was not a standard rectangular pulse

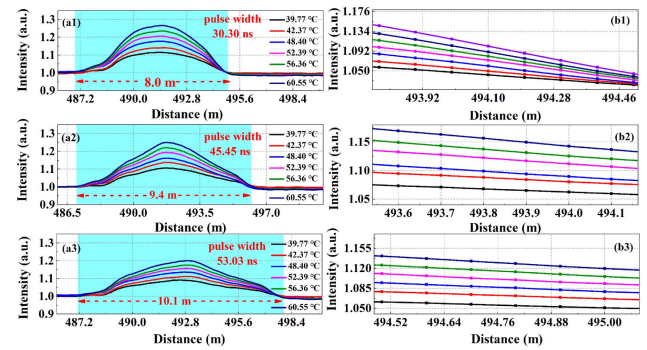


Fig. 6. Distribution of superimposed Raman OTDR traces in the FUT region under the pulse width of (a1) 30.30 ns, (a2) 45.45 ns, and (a3) 53.03 ns. Distribution of superimposed Raman OTDR traces in the slope-assisted region under the pulse width of (b1) 30.30 ns, (b2) 45.45 ns, and (b3) 53.03 ns.

signal, leading to inhomogeneity of the superimposed intensity within the spatial scale of the pulse width. In addition, the rising and falling edges of the pulsed laser affected the smoothness of the Raman OTDR curve.

The influence of the pulse width on the spatial scale of the superimposed Raman OTDR trace in the FUT region was investigated. As shown in Figs. 6(a1)–6(a3), the blue area represents the spatial length where the superimposed Raman signal is modulated by the FUT temperature. The experimental results confirmed the spatial length of the superimposed Raman signal affected by the FUT to be longer than the real length of the FUT area, as elaborated upon in Section 2.A. This indicates that the spatial length of the superimposed Raman signal affected by the FUT area is the FUT length plus the pulse width, as shown in Fig. 7—that is, it shows that the spatial length of the Raman scattered signal is affected by the temperature of the FUT area, the experimental results agreeing with the theoretical analysis and simulation results.

Figures 6(b1)–6(b3) show the distribution of the superimposed Raman OTDR curves in the slope-assisted region. The slope-assisted coefficients (Φ_{slope}) can be calculated using Eq. (10). The relationship between Φ_{slope} and the FUT temperature (T_{FUT}) was also experimentally examined, with pulse widths of 30.30, 45.45, 53.03, and 55.56 ns, respectively,

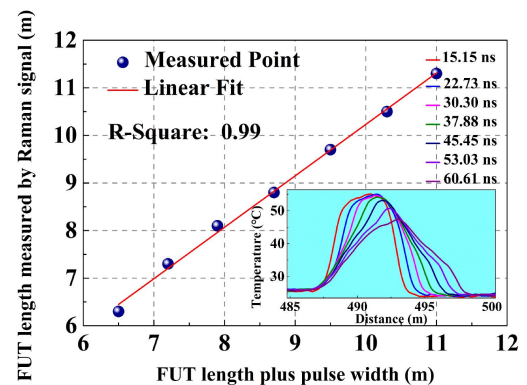


Fig. 7. Relationship between the pulse width and FUT length as measured by Raman signal.

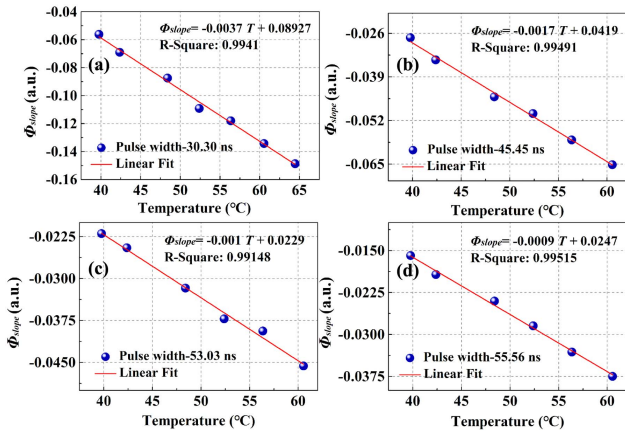


Fig. 8. Relationship between the slope-assisted coefficients and the FUT temperature under the pulse width of (a) 30.30 ns, (b) 45.45 ns, (c) 53.03 ns, and (d) 55.56 ns.

being injected into the FUT. Figures 8(a)–8(d) show the relationship between Φ_{slope} and T_{FUT} . The blue points are the Φ_{slope} values calculated from the experiment, the red line being the fitting curve under different temperature conditions (39.77°C, 42.37°C, 48.40°C, 52.39°C, 56.36°C, and 60.55°C, respectively). The experimental results show that Φ_{slope} and T_{FUT} present a linear function in the slope-assisted region. Consequently, the actual temperature information of the FUT region can be demodulated using the calculated slope-assisted coefficients. In addition, the slopes of the linear function are related to the pulse width—in particular, the slope shows a gradually increasing trend with increase in the pulse width. In practical applications, when the pulse width of the system is fixed, the slope-assisted equation can be determined.

Furthermore, the relationships between Φ_{slope} and T_{FUT} under different FUT lengths were studied. Figures 9(a1)–9(c1) show the distribution of the superimposed Raman OTDR traces under different FUT lengths (6.0, 4.8, and 2.5 m,

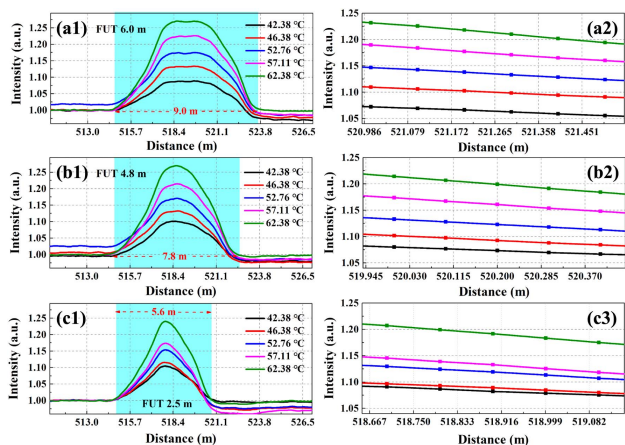


Fig. 9. Distribution of superimposed Raman OTDR traces in the FUT region under the FUT with length of (a1) 6.0 m, (b1) 4.8 m, and (c1) 5.6 m. Distribution of superimposed Raman OTDR traces in the slope-assisted region under the FUT with length of (a2) 6.0 m, (b2) 4.8 m, and (c2) 5.6 m.

respectively). In the experiment, the pulse width was fixed at 30.30 ns. The results show that superimposed Raman OTDR curves deteriorate markedly when the spatial length of the pulse width is larger than the length of the FUT, as shown in Fig. 9(c1). The temperature demodulation of the system was restricted to the use of this degraded Raman OTDR curve. Figures 9(a2)–9(c2) shows the distribution of partially superimposed Raman OTDR traces in the slope-assisted area. Φ_{slope} can also be calculated using Eq. (10).

The relationship between Φ_{slope} and T_{FUT} is shown in Fig. 10. The blue dots represent Φ_{slope} , the red line being the fitting curve. The experimental results show that the slope-assisted coefficients and temperature of the FUT area also exhibit a linear relationship. Most importantly, the results show that the three fitting curves are essentially the same, proving that the linear function depends on the FUT length.

C. Temperature Measurement Results in a Centimeter-Level Spatial Scale

In the initial stage of a fire, the fire source is usually small, and the temperature does not increase quickly. This is the best time to extinguish it. However, the meter-level spatial resolution of the system will cause this temperature variation information to be submerged in the average temperature data within the pulse width scale. To experimentally demonstrate the measurement performance of the proposed slope-assisted method on a centimeter-level spatial scale, a micro-scale temperature measurement experiment was conducted. In the experiment, a cigarette lighter was used to heat the optical fibers—that is, it could set the temperature variation region of the FUT to 1.0 cm, as shown in Fig. 11(a), the core temperature of the flame able to reach 200°C. The pulse width of the system used in the experiment was 53.0 ns, its theoretical spatial resolution being 5.3 m. Limited by the spatial resolution, the temperature of the FUT was 36.56°C and was demodulated using a conventional demodulation method, as shown in Fig. 11(a). However, the conventional Raman demodulation method cannot accurately monitor the temperature in such a small area. Fortunately, the actual temperature signal under the same

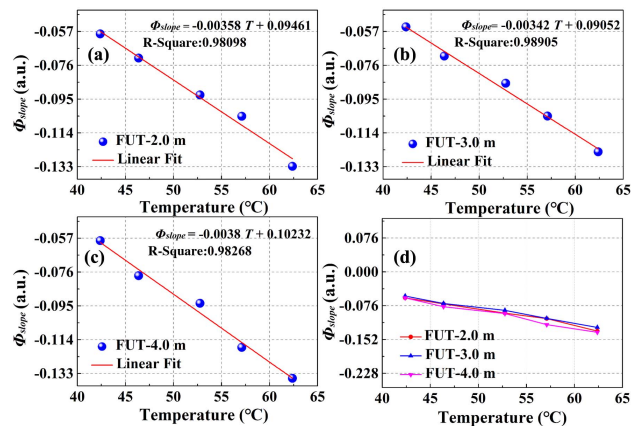


Fig. 10. Relationship between the slope-assisted coefficients and the FUT temperature under FUT lengths of (a) 2.0 m, (b) 3.0 m, and (c) 4.0 m. (d) Comparative results based on the different FUT lengths.

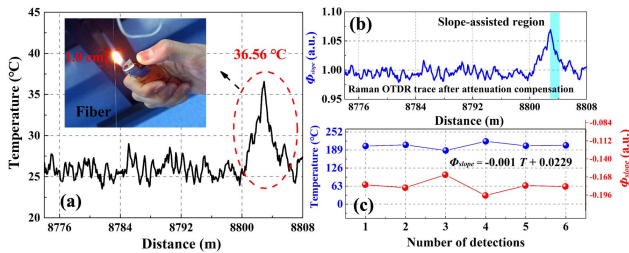


Fig. 11. Temperature measurement results at a centimeter-level spatial scale detected using a conventional demodulation method and the slope-assisted demodulation method. (a) Results measured using the conventional demodulation method. (b) Distribution of superimposed Raman OTDR trace after attenuation compensation. (c) Results measured using the slope-assisted coefficients.

conditions can be accurately demodulated using the proposed slope-assisted scheme.

Figure 11(b) shows the distribution of the superimposed Raman OTDR trace after attenuation compensation. Figure 11(c) shows the slope-assisted coefficients and calculated temperature. Among them, the slope-assisted coefficients could be calculated in the slope-assisted area, being -0.18 , -0.1845 , -0.1645 , -0.1966 , -0.1812 , and -0.1827 in six repetitive experiments, as shown by the red dots in Fig. 11(b). The corresponding demodulation temperature values were also calculated from the slope-assisted equation, being 202.9°C , 207.4°C , 187.4°C , 219.5°C , 204.1°C , and 205.8°C , respectively, as shown by the blue dots in Fig. 11(b), the demodulated temperature results being consistent with the temperature of the flame. This proved that the proposed slope-assisted scheme could accurately demodulate the temperature information on a centimeter-level spatial scale.

4. CONCLUSION

A novel optical scheme for Raman distributed optical fiber sensing was proposed to improve the capability of temperature monitoring in the micro-scale region. In this work, the pulse transmission feature in the temperature variation area of the sensing fiber and the superposition characteristics of the Raman OTDR signal were first theoretically analyzed and then simulated. The results showed that the true length and position information of the FUT could be demodulated by the spatial length of the rising edge of the Raman OTDR trace. Moreover, the spatial length of the Raman OTDR trace affected by the FUT area was the FUT length plus the pulse width. This analysis was enabled by a detailed theoretical analysis of the system's limitations and an optimization process that provided the best possible measurement performance. The theoretical analysis performed in the current study could be a useful tool for designing a distributed optical fiber sensor based on the OTDR principle, such as BOTDR, BOTDA, and Rayleigh-OTDR systems.

A slope-assisted sensing principle and scheme were also proposed and experimentally demonstrated using Raman distributed optical fiber sensing. The falling edge of the superimposed Raman OTDR curve was defined as the slope-assisted detection area in the FUT. The temperature variation information

along the FUT could be demodulated using the proposed slope-assisted coefficients. The experiment showed that the slope-assisted scheme could achieve an accurate measurement in a region with centimeter-level spatial scale, even if the spatial resolution of the system was at the meter-level scale. The results obtained demonstrated a deep understanding of pulsed laser transmission and scattering signal superposition, which can lead to a significant performance improvement in optical fiber sensing. To the best of our knowledge, this is the first demonstration of Raman distributed optical fiber sensing in a centimeter-level spatial measurement region. In the future, we will further optimize the signal to noise ratio (SNR) of the system based on an optical coding modulation scheme.

Funding. National Natural Science Foundation of China (61875146, 62075151, 62075153, 62105234); Key R&D Program (high-tech field) of Shanxi Province (201803D121064, 201803D31044, 201903D121177); Patent Promotion and Exploitation Program of Shanxi Province (20200734); Sanjin Scholar; Shanxi "1331 Project" Key Innovative Research Team; Transformation of Scientific and Technological Achievements Programs of Higher Education Institutions in Shanxi.

Disclosures. The authors declare no conflicts of interest.

Data Availability. Data underlying the results presented in this paper are not publicly available at this time but may be obtained from the authors upon reasonable request.

REFERENCES

- M. A. Soto, J. A. Ramírez, and L. Thévenaz, "Intensifying the response of distributed optical fibre sensors using 2D and 3D image restoration," *Nat. Commun.* **7**, 10870 (2016).
- X. Z. Sun, Z. S. Yang, X. B. Hong, S. Zaslowski, S. Wang, M. A. Soto, X. Gao, J. Wu, and L. Thévenaz, "Genetic-optimised aperiodic code for distributed optical fibre sensors," *Nat. Commun.* **11**, 5774 (2020).
- D. M. Chow, Z. Yang, M. A. Soto, and L. Thévenaz, "Distributed forward Brillouin sensor based on local light phase recovery," *Nat. Commun.* **9**, 2990 (2018).
- Z. W. Zhan, M. Cantono, V. Kamalov, A. Mecozzo, R. Muller, S. Yin, and J. C. Castellanos, "Optical polarization-based seismic and water wave sensing on transoceanic cables," *Science* **371**, 931–936 (2021).
- Y. K. Dong, C. Pang, Z. J. Hua, D. W. Zhou, H. Y. Zhang, L. Chen, and X. Y. Bao, "Optomechanical time-domain analysis based on coherent forward stimulated Brillouin scattering probing," *Optica* **7**, 176–184 (2020).
- Z. Zhao, H. Wu, J. Hu, K. Zhu, Y. L. Dang, Y. X. Yan, M. Tang, and C. Lu, "Interference fading suppression in Phi-OTDR using space-division multiplexed probes," *Opt. Express* **29**, 15452–15462 (2021).
- Z. L. Zhang, Y. G. Lu, J. Q. Peng, and Z. Y. Ji, "Simultaneous measurement of temperature and acoustic impedance based on forward Brillouin scattering in LEAF," *Opt. Lett.* **46**, 1776–1779 (2021).
- J. L. Jiang, Z. N. Wang, Z. T. Wang, Z. J. Qiu, C. Y. Liu, and Y. Y. Rao, "Continuous chirped-wave phase-sensitive OTDR," *Opt. Lett.* **46**, 686–688 (2021).
- A. Leal-Junior, C. Díaz, A. Frizera, H. Lee, K. Nakamura, Y. Mizuno, and C. Marques, "Highly sensitive fiber-optic intrinsic electromagnetic field sensing," *Adv. Photon. Res.* **2**, 2000078 (2021).
- X. T. Lou, Y. B. Feng, S. H. Yang, and Y. K. Dong, "Ultra-wide-dynamic-range gas sensing by optical pathlength multiplexed absorption spectroscopy," *Photon. Res.* **9**, 193–201 (2021).

11. Y. Zhao, Y. Qi, H. L. Ho, S. F. Gao, Y. Y. Wang, and W. Jin, "Photoacoustic Brillouin spectroscopy of gas-filled anti-resonant hollow-core optical fibers," *Optica* **8**, 532–538 (2021).
12. S. Xie, A. Sharma, M. Romodina, N. Joly, and P. St.J. Russell, "Tumbling and anomalous alignment of optically levitated anisotropic microparticles in chiral hollow-core photonic crystal fiber," *Sci. Adv.* **7**, 6053–6062 (2021).
13. H. T. Zhu, L. W. Zhan, Q. Dai, B. Xu, Y. Chen, Y. Q. Lu, and F. Xu, "Self-assembled wavy optical microfiber for stretchable wearable sensor," *Adv. Opt. Mater.* **9**, 2002206 (2021).
14. H. Chen, M. Buric, P. R. Ohodnicki, J. Nakano, B. Liu, and B. T. Chorpening, "Review and perspective: sapphire optical fiber cladding development for harsh environment sensing," *Appl. Phys. Rev.* **5**, 011102 (2018).
15. X. Wang, J. F. Jiang, S. Wang, K. Liu, and T. G. Liu, "All-silicon dual-cavity fiber-optic pressure sensor with ultralow pressure-temperature cross-sensitivity and wide working temperature range," *Photon. Res.* **9**, 521–529 (2021).
16. B. Lu, B. Y. Wu, J. F. Gu, J. Q. Yang, K. Gao, Z. Y. Wang, L. Ye, Q. Ye, R. H. Qu, X. B. Chen, and H. W. Cai, "Distributed optical fiber hydrophone based on Φ -OTDR and its field test," *Opt. Express* **29**, 3147–3162 (2021).
17. S. Gao, Y. Wang, W. Ding, Y. Hong, and P. Wang, "Conquering the Rayleigh scattering limit of silica glass fiber at visible wavelengths with a hollow-core fiber approach," *Laser Photon. Rev.* **14**, 1900241 (2020).
18. V. Fuertes, N. Grégoire, P. Labranche, S. Gagnon, and Y. Messaddeq, "Engineering nanoparticle features to tune Rayleigh scattering in nanoparticles-doped optical fibers," *Sci. Rep.* **11**, 9116 (2021).
19. Z. Zhang, Y. Lu, J. Peng, and Z. Ji, "Simultaneous measurement of temperature and acoustic impedance based on forward Brillouin scattering in LEAF," *Opt. Lett.* **46**, 1776–1779 (2021).
20. Z. Li, Y. Zhou, B. Jiang, and J. Zhao, "Phase fluctuation cancellation for coherent detection BOTDA fiber sensors based on optical subcarrier multiplexing," *Opt. Lett.* **46**, 757–760 (2021).
21. Z. Zhang, H. Wu, C. Zhao, and M. Tang, "High-performance Raman distributed temperature sensing powered by deep learning," *J. Lightwave Technol.* **39**, 654–659 (2021).
22. Y. S. Muanenda, M. Taki, T. Nannipieri, A. Signorini, C. J. Oton, F. Zaidi, I. Toccafondo, and F. Di Pasquale, "Advanced coding techniques for long-range Raman/BOTDA distributed strain and temperature measurements," *J. Lightwave Technol.* **34**, 342–350 (2016).
23. J. Li, Q. Zhang, Y. Xu, M. J. Zhang, J. Z. Zhang, L. J. Qiao, M. M. Promi, and W. Tao, "High-accuracy distributed temperature measurement using difference sensitive-temperature compensation for Raman-based optical fiber sensing," *Opt. Express* **27**, 38163–38196 (2019).
24. Y. Xu, J. Li, M. Zhang, T. Yu, B. Yan, X. Zhou, F. Yu, J. Zhang, L. Qiao, T. Wang, and S. Gao, "Pipeline leak detection using Raman distributed fiber sensor with dynamic threshold identification method," *IEEE Sens. J.* **20**, 7870–7877 (2020).
25. A. Datta, H. Mamidala, D. Venkitesh, and B. Srinivasan, "Reference-free real-time power line monitoring using distributed anti-Stokes Raman thermometry for smart power grids," *IEEE Sens. J.* **20**, 7044–7052 (2019).
26. J. Li, B. Q. Yan, M. J. Zhang, J. Z. Zhang, B. Q. Jin, Y. Wang, and D. Wang, "Long-range Raman distributed fiber temperature sensor with early warning model for fire detection and prevention," *IEEE Sens. J.* **19**, 3711–3717 (2019).
27. J. Q. Wang, Z. Y. Li, X. L. Fu, X. Gui, J. Zhan, H. H. Wang, and D. S. Jiang, "High-sensing-resolution distributed hot spot detection system implemented by a relaxed pulse width," *Opt. Express* **28**, 16045–16056 (2020).
28. Y. Liu, L. Ma, C. Yang, W. Tong, and Z. Y. He, "Long-range Raman distributed temperature sensor with high spatial and temperature resolution using graded-index few-mode fiber," *Opt. Express* **26**, 20562–20571 (2018).
29. M. A. Soto, N. Nannipieri, A. Signorini, A. Lazzeri, and F. D. Pasquale, "Raman-based distributed temperature sensor with 1 m spatial resolution over 26 km SMF using low-repetition-rate cyclic pulse coding," *Opt. Lett.* **36**, 2557–2559 (2011).
30. J. Li, X. X. Zhou, Z. T. Yin, C. Y. Wang, Y. Xu, J. Z. Zhang, and M. J. Zhang, "Reconstruction compression correlation demodulation for Raman optical time domain reflection," *Adv. Photon. Res.* **2**, 2100047 (2021).
31. C. Pandian, M. Kasinathan, S. Sosamma, C. B. Rao, T. Jayakumar, N. Murali, and B. Raj, "Single-fiber grid for improved spatial resolution in distributed fiber optic sensor," *Opt. Lett.* **35**, 1677–1679 (2010).
32. M. Sun, Y. Tang, S. Yang, J. Li, S. Markus, and F. Dong, "Fire source localization based on distributed temperature sensing by a dual-line optical fiber system," *Sensors* **16**, 829 (2016).